RESEARCH ARTICLE

A 3D two-point method for whole-brain water content and relaxation time mapping: Comparison with gold standard methods

Melissa Schall[1], Markus Zimmermann[1], Elene Iordanishvili[1], Yun Gu[1], N. Jon Shah[1,2,3,4], Ana-Maria Oros-Peusquens[1]*

1 Institute of Neuroscience and Medicine 4 (INM-4), Research Centre Jülich, Jülich, Germany, **2** Institute of Neuroscience and Medicine 11 (INM-11), Research Centre Jülich, Jülich, Germany, **3** Jülich Aachen Research Alliance (JARA-BRAIN)—TranslationalMedicine, Aachen, Germany, **4** Department of Neurology of the RWTH Aachen University, Aachen, Germany

* a.m.oros-peusquens@fz-juelich.de

Abstract

Quantitative imaging of the human brain is of great interest in clinical research as it enables the identification of a range of MR biomarkers useful in diagnosis, treatment and prognosis of a wide spectrum of diseases. Here, a 3D two-point method for water content and relaxation time mapping is presented and compared to established gold standard methods. The method determines free water content, H_2O, and the longitudinal relaxation time, T_1, quantitatively from a two-point fit to the signal equation including corrections of the transmit and receive fields. In addition, the effective transverse relaxation time, T_2^*, is obtained from an exponential fit to the multi-echo signal train and its influence on H_2O values is corrected. The phantom results obtained with the proposed method show good agreement for H_2O and T_1 values with known and spectroscopically measured values, respectively. The method is compared *in vivo* to already established gold standard quantitative methods. For H_2O and T_2^* mapping, the 3D two-point results were compared to a measurement conducted with a multiple-echo GRE with long TR and T_1 is compared to results from a Look-Locker method, TAPIR. *In vivo* results show good overall agreement between the methods, but some systematic deviations are present. Besides an expected dependence of T_2^* on voxel size, T_1 values are systematically larger in the 3D approach than those obtained with the gold standard method. This behaviour might be due to imperfect spoiling, influencing each method differently. Results for H_2O differ due to differences in the saturation of cerebrospinal fluid and partial volume effects. In addition, ground truth values of *in vivo* studies are unknown, even when comparing to *in vivo* gold standard methods. A detailed region-of-interest analysis for H_2O and T_1 matches well published literature values.

(gschmalzing@ukaachen.de, ekaachen@ukaachen.
de).

Introduction

Despite the fact that nuclear magnetic resonance (NMR) is routinely used as a quantitative, analytical technique and its imaging counterpart, magnetic resonance imaging (MRI), has revolutionised clinical medicine, quantitative MR imaging has been slow to find its way into the clinic. This is, to some extent, due to the long acquisition times, the generally lower resolution of the maps obtained when compared to routine anatomical imaging and the need for elaborate post-processing. However, despite these limitations, quantitative MR imaging can be advantageous when it comes to e.g. investigating pathology. In brain tumour imaging, it has been shown that the longitudinal relaxation time, T_1, as well as the transverse relaxation time, T_2, are highly relevant (see e.g. [1]). Recent publications report that T_1 and T_2^*, which reflects T_2 under the influence of magnetic heterogeneity, as well as free water content, H_2O, change systematically within brain tumour tissue compared to healthy tissue [1,2]. Here, free water content means the proton density of the visible free water proton density as described in [3]. As several recent publications indicate (e.g. [1,2,4–6]), there is increased interest in promoting quantitative imaging for several applications.

Most quantitative MR imaging methods presented in the literature and used in various studies utilise 2D sequences, as in general 2D imaging is faster than 3D [5,7–11]. However, there are significant benefits offered by 3D, as compared to 2D imaging: These include the increase in the signal-to-noise ratio (SNR) due to additional sampling, a purely rectangular slice profile, eliminating the need for slice profile corrections in 2D methods (e.g. [11]) and generally higher and isotropic resolution minimising partial volume effects (PVE). Despite these benefits, a major problem associated with 3D imaging is the requirement for a short repetition time, TR, compared to 2D methods. Generally, this does not allow for full relaxation of the magnetisation, which is important in quantitative water content mapping, and elaborated correction techniques become necessary, which correct the influence of imperfect RF spoiling (e.g. [11,12]). Another shortcoming of the published 3D mapping methods is that elaborate corrections for the influence of imperfect RF spoiling become necessary. Previously, this has been either neglected [13] or performed mathematically [14,15] instead of being measured, due to measurement time requirements. However, with the recent development of a fast, 3D B_1^+ calibration method, Actual Flip Angle Imaging (AFI) [16], this gap has been closed.

Here, we present a 3D two-point (3D2P) method for high-resolution and isotropic H_2O and relaxation time mapping, in which H_2O, T_1 and T_2^* are determined from a fit to the signal equation including several corrections. The method is based on a 3D multi-echo gradient echo (meGRE) sequence, which benefits from an efficient readout-scheme and has low specific absorption rates (SAR), which is particularly important at high field strengths. In contrast to other implementations (e.g. DESPOT [13]), TR is chosen to be long enough to allow for sampling of the echo train up to at least T_2^*. In practice, we chose TR = 50ms, which allows for accurate T_2^* mapping and also minimises contributions from insufficiently spoiled magnetisation. The latter aspect is very important, since insufficient spoiling was shown to have a negative effect on the quantitative power of such methods [12], making the assumed signal equation invalid. The rather long TR for a 3D method was used to acquire 18 echoes and increase the SNR of quantitative maps. The RF transmit field is mapped using a 3D AFI sequence. Given that methods for accurately measuring the receiver profile are rather imprecise and they add to the measurement time, we chose to use a Statistical Parametric Mapping (SPM12) [17]-based correction to the proton density map to determine B_1^- [2]. From the available data, methods using the correlation between H_2O and T_1 to eliminate B_1^- effects could also be used retrospectively. Free water content is derived from the corrected proton density of the visible free water.

The parameter space of two-point methods is very large, including many parameters which may be changed in order to improve different aspects of the method. We have used the specified constraint of the repetition time (TR approximately equal to T_2^*) and optimised the flip angles to increase the reliability and accuracy of H_2O and T_1. This was done based on signal equation assuming perfect spoiling and Monte Carlo simulations (cf. S1 Text and S1 Fig).

The accuracy of the method presented was investigated using phantom experiments, whereas the reliability was investigated by ten test-retest measurements of the same subject. In addition, the results obtained with the proposed method were compared *in vivo* on a cohort of 10 volunteers to results from gold standard methods for H_2O, T_2^* and T_1 mapping. Finally, a region-of-interest (ROI) analysis for H_2O and T_1 was performed, allowing comparison to literature results.

Material and methods

Data acquisition

The test-retest measurements were conducted on a single female subject (28 years), and the *in vivo* comparison to gold standard methods performed on ten male subjects between 23–32 years of age (mean age 27 years and a standard deviation of 3 years). Subjects were included after they gave prior, written informed consent to the Forschungszentrum Jülich; this specific study was approved in accordance with institutional guidelines by the Ethics Committee of the RWTH Aachen University ("Entwicklung und Optimierung von Bildgebungssequenzen und Protokollen für die MRT bei Feldstärken kleiner 4 Tesla", ethics number EK 226/09).

All measurements were conducted on a 3T Siemens Tim Trio whole-body scanner equipped with a gradient coil with maximum field strengths of 40mT/m on each axis. An RF body coil with homogeneous RF field distribution over the head was used for RF transmit. A 32-element phased-array head coil was used for signal detection. During the test-retest measurements, the volunteer was taken out of the scanner after each time point. The positioning procedure and shimming were repeated each time.

The MR protocol consists of three separate acquisitions: two 3D multiple-echo gradient echo sequences (meGRE), which are M_0- and T_1-weighted respectively, and an AFI sequence to map the transmit field B_1^+. In the present implementation, the 3D meGRE sequence offered by the manufacturer (Siemens) was modified to allow for a higher number of echoes. For the comparison study, the imaging parameters for the meGREs included: repetition time of TR = 50ms, α = 7˚ and 40˚, 18 echoes with TE_1 = 2.2ms and dTE = 2.55ms, one slab with 192 slices, slice oversampling of 33.3%, 1mm isotropic resolution, matrix size 162×192×192, bandwidth 650Hz/px, GRAPPA parallel imaging with an acceleration factor of 2 and 24 reference lines, phase and slice partial Fourier factor of 6/8, acquisition time of 8:44 min per scan. During the test-retest measurements the resolution was reduced to 1×1×2 mm³, while keeping the remaining parameters constant, resulting in a total acquisition time of 4:19 min per scan. The values chosen for TR and α were optimised using Monte Carlo simulations (cf. S1 Text and S1 Fig). Using proper slab selection prevents field inhomogeneities when setting the field-of-view (FOV) in the centre of the slab. As the edges of the slab profile have lower precision and accuracy, which also results from non-perfect flip angles, a rectangular profile was ensured by employing slice oversampling. The acquisition parameters of the AFI sequence were set as follows: TR_1/TR_2 = 5 with TR_1 = 125ms, α = 40˚, (3.1×3.1×4)mm³ resolution, one slab with 48 slices, 33.3% slice oversampling, base resolution of 64, bandwidth 330Hz/px, 100% phase and slice resolution, FOV equal to the meGREs, phase and slice resolution 100%, GRAPPA parallel imaging with an acceleration

factor of 2 and 24 reference lines, phase and slice partial Fourier factor of 6/8, and acquisition time of 4:00 min. The total acquisition time of the 3D2P method with the listed parameters was thus 21:28 min (12:50 min for the test-retest measurements).

To compare the resulting H_2O and T_2^* maps, a gold standard 2D meGRE technique is used, which due to its long TR = 10s allows full relaxation of the magnetisation density for practically all T_1 values met in tissue [18]. As only one flip angle and slice profile is used, a T_1 correction becomes unnecessary [2]. Other parameters were: $\alpha = 90°$, resolution of $(1.0 \times 1.5 \times 1.5)mm^3$ with 1mm slice gap (in-plane resolution is interpolated to $1 \times 1mm^2$ during post-processing), base resolution of 192, bandwidth 280Hz/px, 75% phase resolution, 32 echoes with $TE_1 = 3.84ms$ and $dTE = 4.08ms$, partial Fourier sampling was set to 6/8 and GRAPPA acceleration was used with an acceleration factor of 2 and 24 reference lines, and acquisition time was TA = 7:36 min.

For comparison of T_1, we used a Look-Locker method, TAPIR [7,8] and an additional measurement which maps the inversion efficiency (IE) was included. Eight slices with and above the lateral ventricles were acquired. Measurement parameters were set as follows: $(1.0 \times 1.0 \times 2.0)mm^3$ resolution $((3.1 \times 3.1 \times 2.0)mm^3$ for IE), distance factor of 300%, base resolution of 64, bandwidth of 630Hz/px both plus 6mm slice gap, 100% phase resolution, the FOV was set to match the 3D2P method, TR = 20.4ms, TE = 8.13ms (segmented read-out with EPI factor of 3), $\alpha = 32°$, 25 sample points on the inversion recovery curve, GRAPPA with an acceleration factor of 2 and 24 reference lines. The acquisition time was TA = 3:10min for TAPIR and TA = 0:48min for IE mapping.

Theory and processing

All quantitative parameters, H_2O, T_1 and T_2^*, are extracted voxel by voxel from the meGRE signal equation, which is given by

$$S(\text{TE}) = M_0 \cdot \underbrace{e^{-\frac{\text{TE}}{T_2^*}}}_{C_{T_2^*}} \cdot \underbrace{\sin(B_1^+ \alpha_{\text{nom}}) \cdot \frac{1 - e^{-\frac{\text{TR}}{T_1}}}{1 - e^{-\frac{\text{TR}}{T_1} \cdot \cos(B_1^+ \alpha_{\text{nom}})}}}_{C_{T_1, B_1^+, \alpha}} \cdot \underbrace{B_1^-}_{C_{B_1^-}} \tag{1}$$

where M_0 is the magnetisation density, B_1^+ is the transmit and B_1^- is the receive RF field inhomogeneity and $\alpha_{\text{eff}} = B_1^+ \alpha_{\text{nom}}$ describes an effective flip angle depending on the nominal flip angle, α_{nom}. In order to map H_2O quantitatively, the magnetisation density is corrected for the three multiplicative correction factors defined in Eq 1 ($C_{T_2^*}$, $C_{T_1, B_1^+, \alpha}$ and $C_{B_1^-}$). Second, the corrected M_0 map is normalised to the magnetisation density of voxels consisting of 100% water by using a normalisation factor, C_{nom};

$$H_2O = C_{\text{nom}} \cdot M_0 \tag{2}$$

First, the transmit field map was calculated from the known AFI equation [16] via the effective flip angle:

$$\alpha_{\text{eff}} \approx \arccos \frac{rn - 1}{n - r} \tag{3}$$

with $r = S_2/S_1$ and $n = TR_2/TR_1$. Here, TR_1 and TR_2 are the two different repetition times used during the AFI measurement, leading to signals S_1 and S_2. For improved accuracy and numerical stability, the problem is re-formulated and solved iteratively. Since, $B_1^+ = \alpha_{\text{eff}}/\alpha_{\text{nom}}$ the flip angle map needs to be calibrated to the nominal flip angle to yield the final transmit field map.

The T_1 map can be numerically calculated by minimising the differences in the signal equation by solving

$$T_1 = \arg\min_{T_1} \sum_{n=1}^{3} \left| \frac{S_{\alpha_1}(\text{TE}_n)}{C_{T_1,B_1^+,\alpha_1}} - \frac{S_{\alpha_2}(\text{TE}_n)}{C_{T_1,B_1^+,\alpha_2}} \right|^2.$$

(4)

Here, S_{α_1} and S_{α_2} are the signal intensities of the two meGRE and TE_n the n-th echo time. C_{T_1,B_1^+,α_1} is the correction factor for T_1, B_1 and α as introduced in Eq 1. For the T_1 fitting, the first three echoes were used. Using more echoes improves the fit, similar to averaging, and the first echoes have the highest SNR. However, signal reduction due to T_2^* decay has a negative impact on the accuracy of the fit. The choice for three echoes was done empirically in order to avoid signal drop-off at later echoes in regions with high B_0 field inhomogeneities. As both meGRs use the same TE, the residual T_2-weighting is equal in both images and thus does not influence the T_1 calculation. The B_1^+-weighting is supplied by measurement (AFI). This calculation leads to a quantitative T_1 map. All T_1 values exceeding 6s were clipped. The longest T_1 expected for the brain is that of cerebrospinal fluid (CSF) which is below this limit [19].

Thereafter, T_2^* was calculated from the signal decay of the M_0-weighted meGRE using a weighted log-linear fit according to Eq 2 by solving

$$\hat{S}_0, \hat{T}_2^* = \arg\min_{S_0, T_2^*} \sum_{\forall \text{TE}_n \leq \text{TE}_{\max}} |S(\text{TE}_n)| \left| \ln(S(\text{TE}_n)) - \ln(M_0) - \frac{\text{TE}_n}{T_2^*} \right|^2$$

(5)

where TE_n indicates the n-th echo of the meGRE sequence. It was shown that strong field inhomogeneities of B_0 disturb the mono-exponential signal model [20,21]. As the effect of these disturbances increase with time, the fit has to be limited to echo times, where it can be considered negligible. Therefore, a voxel-wise echo time limitation $\text{TE}_{\max}$ was derived based on the gradient of the local magnetic field. Only those echoes TE_n, where $\text{TE}_n < \text{TE}_{\max}$ where subsequently included in the fit. The field gradient was computed from the phase information of the gradient echo images. The quantitative T_2^* map was clipped in order to avoid unreasonable values. Here, $T_2^* \leq 1.5$s was chosen.

The receive field inhomogeneity B_1^- was corrected using the unified segmentation approach of SPM, which is based on brain tissue classification [22]. As the data was initially corrected for transmit field inhomogeneity based on AFI (cf. Eq 3), the remaining inhomogeneity that is corrected for using the unified segmentation approach accounts solely for B_1^-.

The fully corrected and non-normalised M_0 map is given by

$$M_0 = \frac{1}{N} \sum_{n=1}^{N=3} S(\text{TE}_n) \cdot C_{T_2^*}^{-1}(\text{TE}_n) \cdot C_{T_1,B_1^+,\alpha}^{-1} \cdot C_{B_1^-}^{-1}$$

(6)

As only the first three echoes are taken into account, N = 3.

Finally, H_2O was computed from M_0 by normalising to 100% free water according to Eq 2. The normalisation region was chosen as proposed for a 2D two-point water content mapping method [9]. The lateral ventricles, which contain CSF of approximately 100% free water, are taken as normalisation region. The CSF probability map provided by the unified segmentation approach was used as a starting point. In order to include in the normalisation only voxels which are well described by the model, the quantitative T_1 and T_2^* maps were used as further constraints. Only voxels which have a CSF probability of 99% or higher and $T_1 > 2900$ms and $T_2^* > 500$ms are included in the mask. To extract the lateral ventricles from this mask, an ellipsoid is placed around the lateral ventricles, which excludes CSF voxels from the subarachnoid

space. Within this normalisation region the mean value of the corrected M_0 map is taken as normalisation factor, C_{norm}.

The entire post-processing chain is depicted schematically in Fig 1.

Phantom experiments

A multi-compartment cylinder phantom was used to validate the results of the 3D2P method. The phantom contained eight tubes filled with different mixture ratios of H_2O and D_2O. For acquisitions using the proton Larmor frequency (127.8MHz at 3T), D_2O is MRI-invisible so that various H_2O values become detectable. This procedure allows the measurement of H_2O values between 50% and 100%. The H_2O map was normalised based on a tube filled with 100% H_2O. All tubes were doped with different $MnSO_4$ concentrations to shorten the T_1 relaxation times. Reference values for T_1 were obtained by spectroscopic measurements on each tube. For signal detection, a 12-channel phased array coil was used.

Processing

The B_1^+ map was co-registered to the meGRE space. Subsequently, all parameter maps were produced using the post-processing described in Section 2.2. For both, phantom and *in vivo* validation, the same B_1^- correction was applied. For the test-retest measurements, global white matter (WM) and grey matter (GM) values of each quantitative parameter were calculated. To this aim, SPM12 was used to segment the brain and generate specific tissue probability maps, yielding the probability of each voxel belonging to the respective tissue type. Tissue masks were produced from these maps using a probability threshold of 99%. As a parameter indicating the reliability of the method, the standard deviation of the global values of H_2O, T_1 and T_2^* over the whole of WM and GM were derived from the ten time points of the test-retest measurements. For the comparison study, the quantitative maps obtained with the 3D2P method have been co-registered to the resolution of the respective gold standard maps. The final resolution for comparison is therefore the lower one of the reference method, such that the partial voluming effects on the quantitative maps are comparable. The final resolution for comparison is therefore the lower one of the reference method. The co-registration of the T_2^* map introduces erroneous values at the CSF/tissue border due to interpolation and reslicing. Thus, for illustrational purposes the 3D T_2^* map is shown in the native space. Global mean values of WM and GM were calculated using the same tissue masks as mentioned before. The WM and GM histograms for each tissue class were fit by a Gaussian distribution, which provided the information for mean value and standard deviation. After analysing the global *in vivo* tissue values, a more detailed overview of seven GM regions-of-interest (ROI), i.e. temporal, frontal, occipital and parietal lobe as well as putamen, head of caudate and thalamus was provided for H_2O and T_1. For that, SPM12 was used to co-register the quantitative T_1 and H_2O maps of each subject to the 1mm isotropic resolution MNI152 template. In order to select specific GM regions, their segmentation mask in MNI space was multiplied with the GM probability mask with a threshold of 95%. After calculating the mean value and standard deviation of each subject, the weighted mean value was calculated in each ROI. The relatively low resolution of the gold standard methods compared to the MNI template, makes a co-registration to the 1mm^3 isotropic template difficult and prone to error. Thus, the ROI results of the 3D2P methods were compared to literature results. All post-processing was performed off-line using in-house scripts written in Python [23].

Results phantom experiments. The measured values for H_2O content and T_1 are shown in Fig 2. The numerical values were obtained by placing a 3D ROI within each tube.
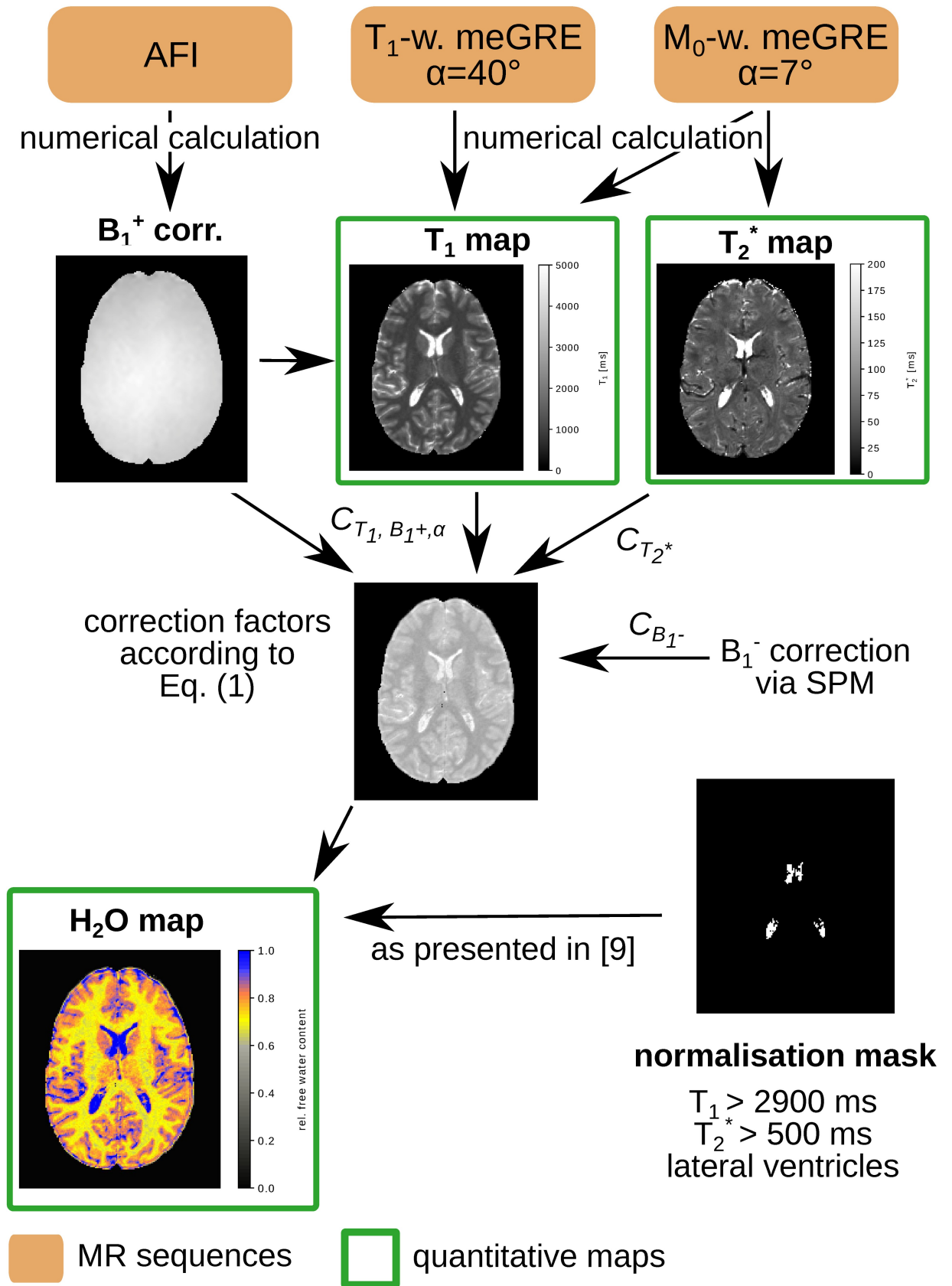
Fig 1. Processing diagram of the 3D2P method. The protocol consists of two 3D meGRE with 7° (M_0-weighting) and 40° (T_1-weighting) and an AFI sequence to map the transmit field, B_1^+. From these sequences a quantitative T_1, T_2^* and H_2O map can be calculated using the post-processing scheme presented.

As can be seen, all values obtained with the 3D mapping method fit well within their standard deviation to the corresponding reference value. In particular, the values of relevance for brain tissue, i.e $H_2O \approx 70$–80% and $T_1 \approx 800$-1600ms are of main interest. The accuracy is determined as the difference between mean value over the ROI and reference value. Thus, for the values most relevant for *in vivo* measurements (tubes 3–6 for H_2O and tubes 4–7 for T_1), the agreement in H_2O content is 0.3–2.1% and for T_1 it is 3-143ms.

In vivo experiments

The test-retest measurements yield a standard deviation of 0.21% (WM) and 0.36% (GM) for H_2O, 6ms (WM) and 8ms (GM) for T_1, and 0.5ms (WM) and 0.4ms (GM) for T_2^*. All values from the single measurement time points are listed in the supporting information (cf. S2 Text, S2 Fig, S1 and S2 Tables).

For the comparison study, we have chosen for illustration purposes maps from a representative healthy volunteer and a slice including various anatomical features.

Free water content comparison. Quantitative H_2O maps obtained with the 3D2P and long TR method, respectively, are shown in Fig 3 for comparison.

Fig 4(A) shows the comparison of H_2O results for all subjects. We plot the mean value of the H_2O distribution within WM and GM obtained with the 3D2P and long TR methods, respectively. The distributions were characterised in the native space. Note that the error bars characterise the width (sigma) of the Gaussian which fits the distribution from each tissue (i.e. global WM and GM) and thus reflects tissue heterogeneity with respect to this parameter and not the accuracy/reliability of the methods. Fig 4(B) depicts the corresponding voxel-wise comparison using the same masks as for the global comparison. The colour visualises the voxel count of each value. Clusters corresponding to WM and GM, respectively, can be clearly
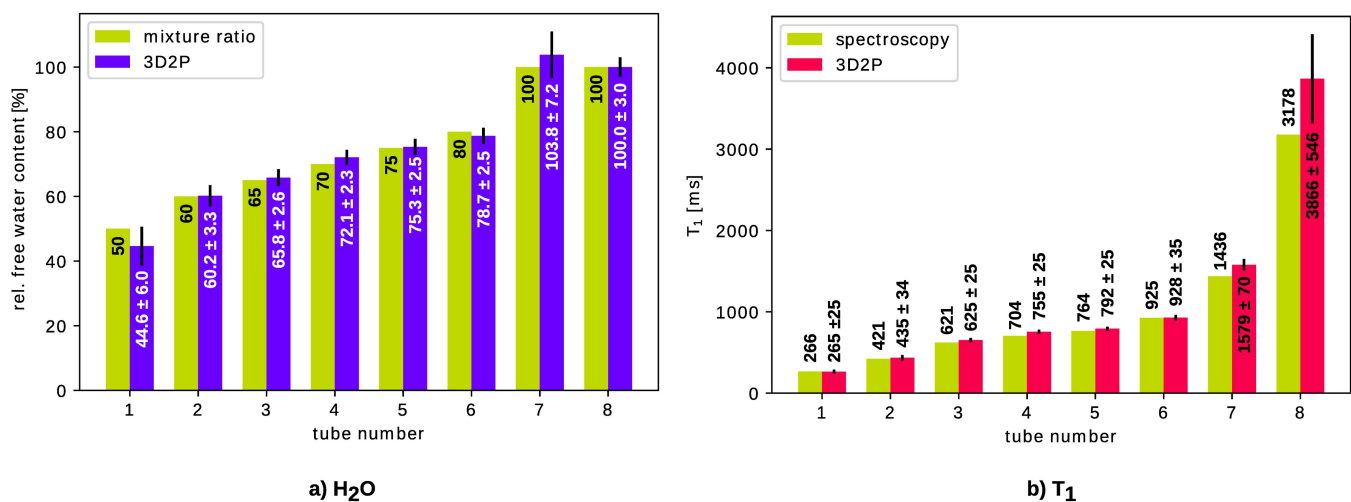

Fig 2. Comparison of quantitative values measured in a multi-compartment cylinder phantom. Reference values are taken as mixture ratios for a) H_2O and spectroscopic values for b) T_1, respectively.
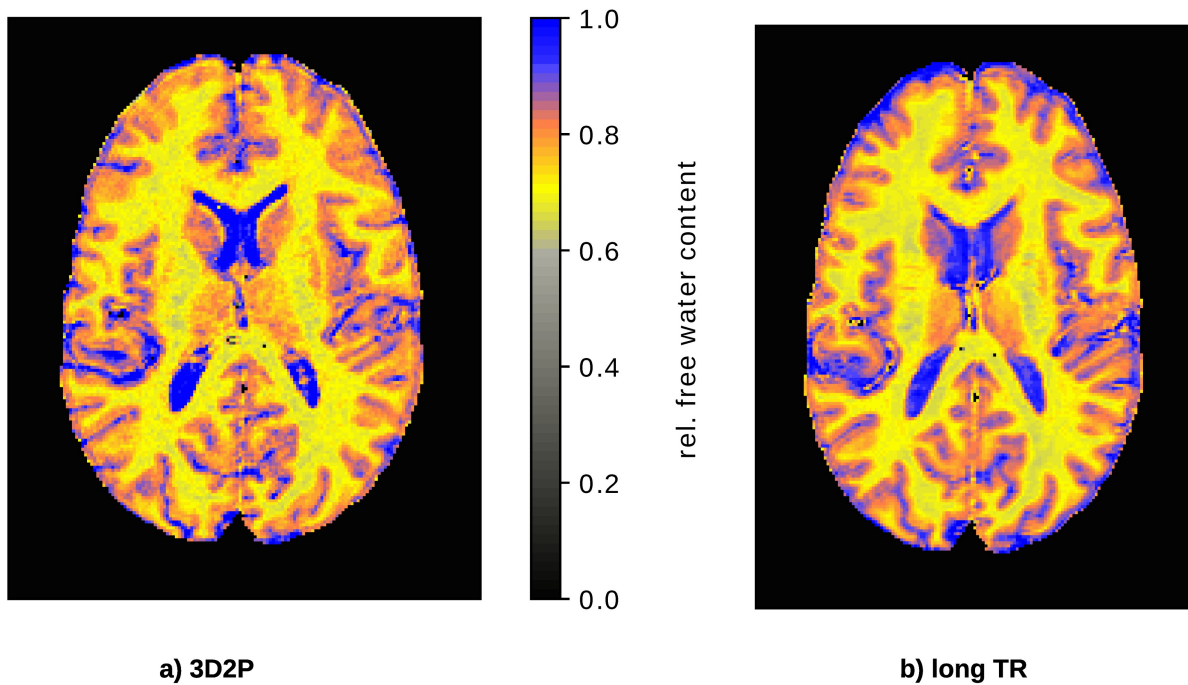
a) 3D2P   **b) long TR**

Fig 3. *In vivo* comparison of the quantitative H$_2$O maps using a) the 3D2P method presented here and b) the long TR reference method.

a) global value comparison   **b) voxel-wise comparison**
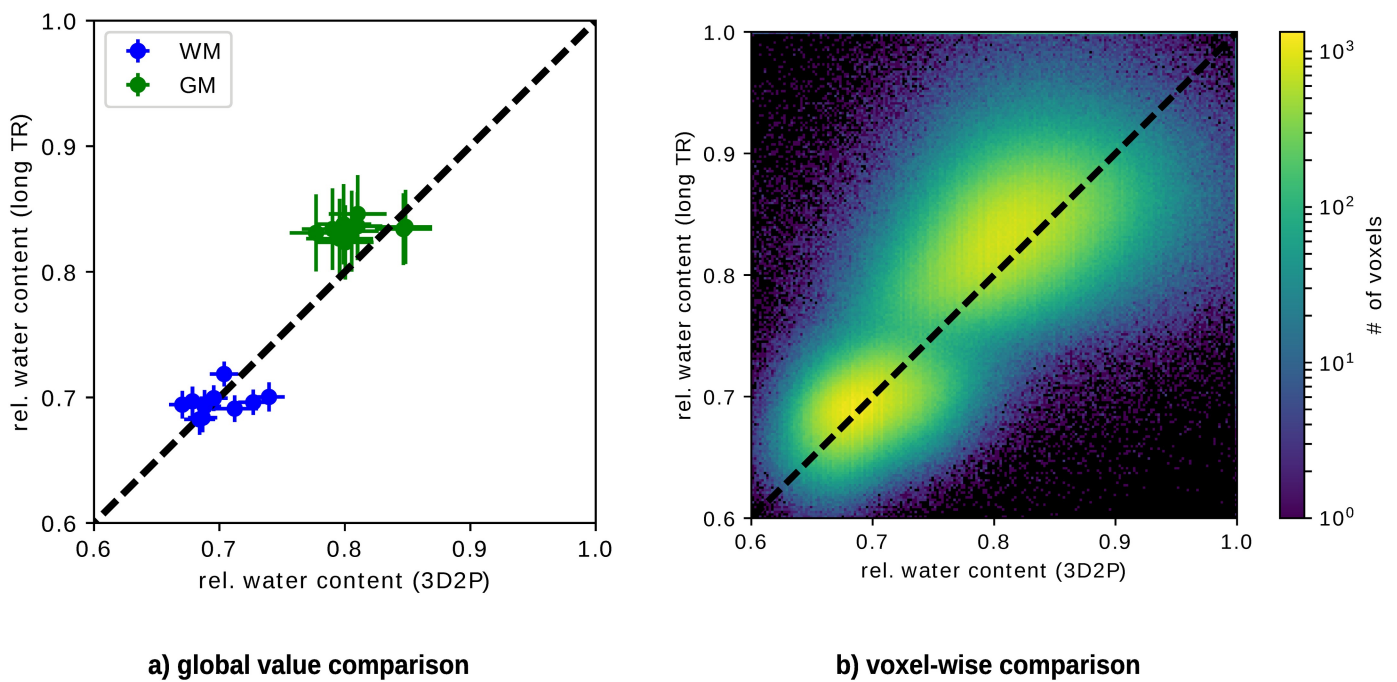
Fig 4. Analytical comparison of quantitative H$_2$O values using 3D2P and long TR method as the gold standard. a) shows the global correlation between the 3D2P and long TR methods, while b) depicts the corresponding voxel-wise analysis.

Table 1. Comparison of H₂O values measured with the 3D2P and the long TR method.

tissue type	H₂O (3D2P) [%]	H₂O (long TR) [%]
WM	69.9±2.1	69.5±1.0
GM	80.8±2.2	83.4±0.6

separated. The WM cluster lies on identity line, whereas the GM cluster is shifted towards higher values in the long TR method.

In addition, the weighted mean values obtained from all subjects are listed in Table 1. As before, a shift of GM can be observed, while the WM mean values match well. However, within their standard deviation the GM values of 3D2P and long TR match. Moreover, all results are in agreement with recently published literature [9].

Fig 5 depicts the cumulative and a representative single subject histogram of H₂O acquired with the 3D2P method. As can be seen, the distribution for WM and GM have clearly distinguishable peaks, which broaden only slightly in the cumulative histogram.

H₂O results of a detailed GM ROI analysis are listed in Table 2 and compared with recently published literature results. Note that the literature values for some ROI, e.g. in thalamus, vary.

T₁ comparison. Both quantitative T₁ maps are depicted in Fig 6. The results of the 3D2P method, calculated at the original resolution and SNR, are co-registered to the images of the TAPIR acquisition and resampled to this lower resolution. Visually, the T₁ map acquired with TAPIR shows a higher contrast-to-noise ratio than the 3D T₁ map. The global and voxel-wise comparison of T₁ values depicted in Fig 7 show that the T₁ obtained with the 3D2P method are slightly higher than the ones acquired with TAPIR. The small, yet consistent trend is also indicated in Table 3. The voxel cluster for WM and GM are distinct and lie close to the identity line, but for TAPIR, the standard deviation of GM is larger than in WM.

As before, the weighted mean values of WM and GM are listed in Table 3. The values differ by a few milliseconds, but match within the first standard deviation and are therefore, highly compatible. Additionally, all results are in agreement with recently published literature [24].

Fig 8 shows the histograms of all subjects compared to a single subject measured with the 3D2P method. The WM and GM peaks are narrow and clearly distinct, indicating a good separation of tissue values.

a) cumulative histogram

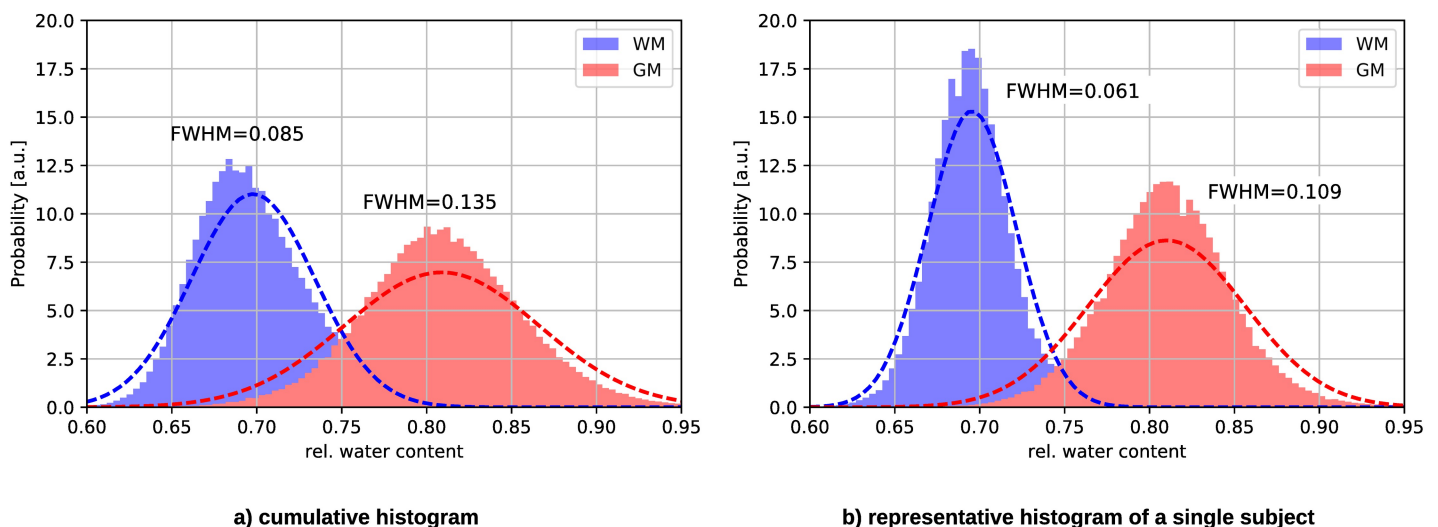**b) representative histogram of a single subject**

Fig 5. H₂O histogram of a) all subjects and b) a representative subject measured with the 3D2P method. The dotted line represents the Gaussian fit to the histograms.

Table 2. Estimated H$_2$O and corresponding literature values in selected GM regions.

GM region	H$_2$O [%]	literature values [%]
temporal lobe	78.9±2.8	82.0±3.1 [9]
frontal lobe	79.9±2.4	81.8±2.8 [24]
occipital lobe	79.7±2.9	83.2±1.7 [24]
parietal lobe	79.6±2.4	83.3±1.5 [24]
		81.1±1.0 [14]
caudate (head)	81.7±2.3	82.1±1.7 [24]
putamen	80.2±2.3	82.7±1.5 [24]
		81.9±1.1 [14]
		82.3±2.6 [25]
		83.1±0.9 [26]
thalamus	79.1±2.2	82.7±1.5 [24]
		79.8±1.0 [26]
		81.0±2.2 [25]

https://doi.org/10.1371/journal.pone.0201013.t002

Analogous to H$_2$O, a detailed ROI analysis was conducted for specific GM regions. The T$_1$ values are listed in Table 4. As can be seen, the results from the proposed method match very well most literature reports.

T$_2$* comparison. Fig 9 compares the T$_2$* results, of both methods. For illustrational purposes, similar slices of both maps were chosen. It can be seen that the visibility of the anatomical structure is improved in the 3D2P method.

As for the other quantities, the T$_2$* tissue values are compared globally (cf. Fig 10A), as well as voxel-wise (cf. Fig 10B). Since the T$_2$* Gaussian distributions for WM and GM are rather broad and overlap, the fit fails to identify two Gaussians. Instead, the mode value is taken as reference WM and GM value and thus, no error bars occur. No specific tissue clusters can be recognised in the voxel-wise analysis (cf. Fig 10B). The mean T$_2$* values obtained with both methods are listed in Table 5. Fig 11 also illustrates the broad WM and GM peaks in the cumulative as well as single subject T$_2$* histogram measured with 3D2P.

Discussion and outlook

We propose here a quantitative method for H$_2$O, T$_1$ and T$_2$* mapping and assess its performance *in vivo* in comparison to gold standard methods. For the *in vivo* analysis, long TR and TAPIR were chosen as gold standard methods because of their high accuracy as compared to competitive methods, e.g. DESPOT [13] and fingerprinting methods [31]. It is well known that imaging with a long repetition time delivers images which mainly reflect the magnetisation density of MR-visible water [3]. However, a number of corrections are still required in order to obtain the quantitative H$_2$O from these images. The mapping method chosen here as the gold standard uses a long TR value of 10s, which is sufficiently long to ensure T$_1$ saturation effects in brain tissue are negligible and still short enough to allow for clinical use [2]. The T$_2$* correction is based on exponential fitting of the multi-echo train up to a voxel-specific maximum echo time chosen to minimize the effect of the off-resonance magnetic field. All other corrections are multiplicative and can be treated as a bias field correction, for example as implemented in SPM. Conversion to H$_2$O values is performed by calibration to CSF, considered to consist of 100% MR-visible water. Very important for quantitative imaging, where noise influence is detrimental to both accuracy and reliability, the design of the method maximises SNR, by detecting the whole available magnetisation following a 90° pulse. The
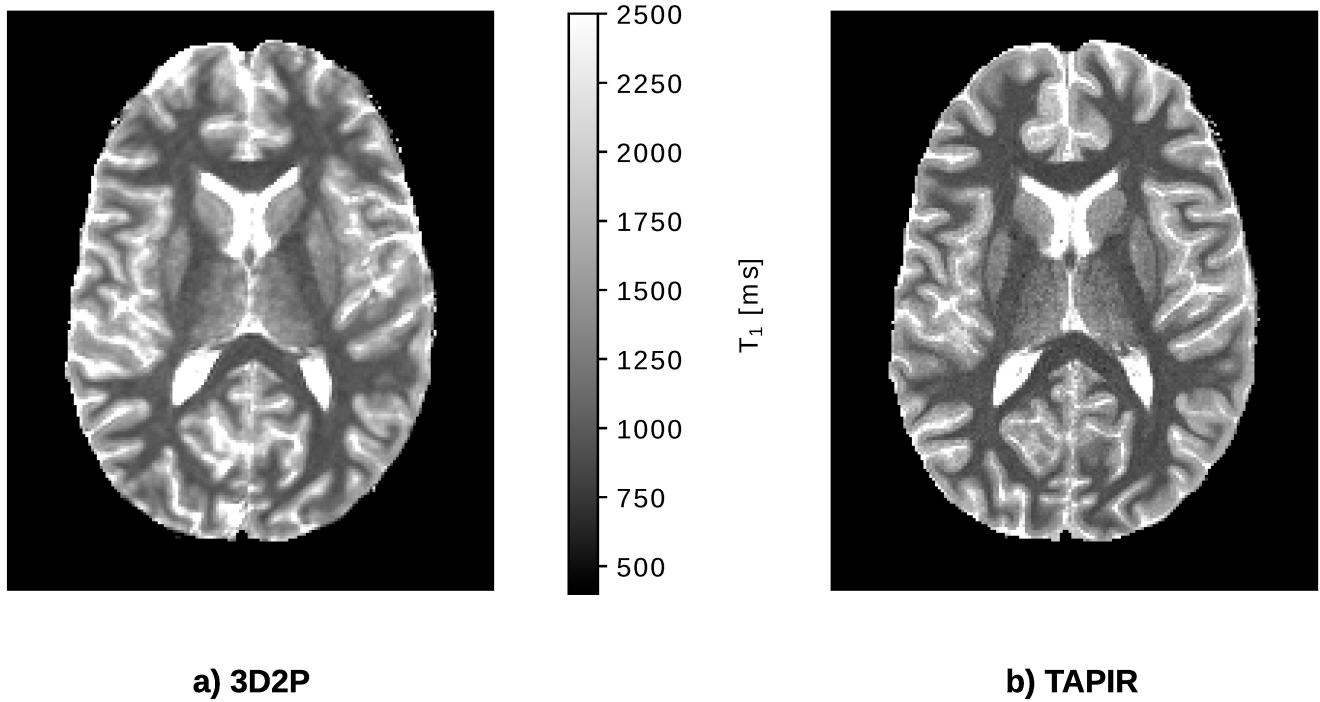
a) 3D2P **b) TAPIR**

Fig 6. *In vivo* comparison of the quantitative T$_1$ maps using the 3D2P method and TAPIR as the gold standard.

https://doi.org/10.1371/journal.pone.0201013.g006

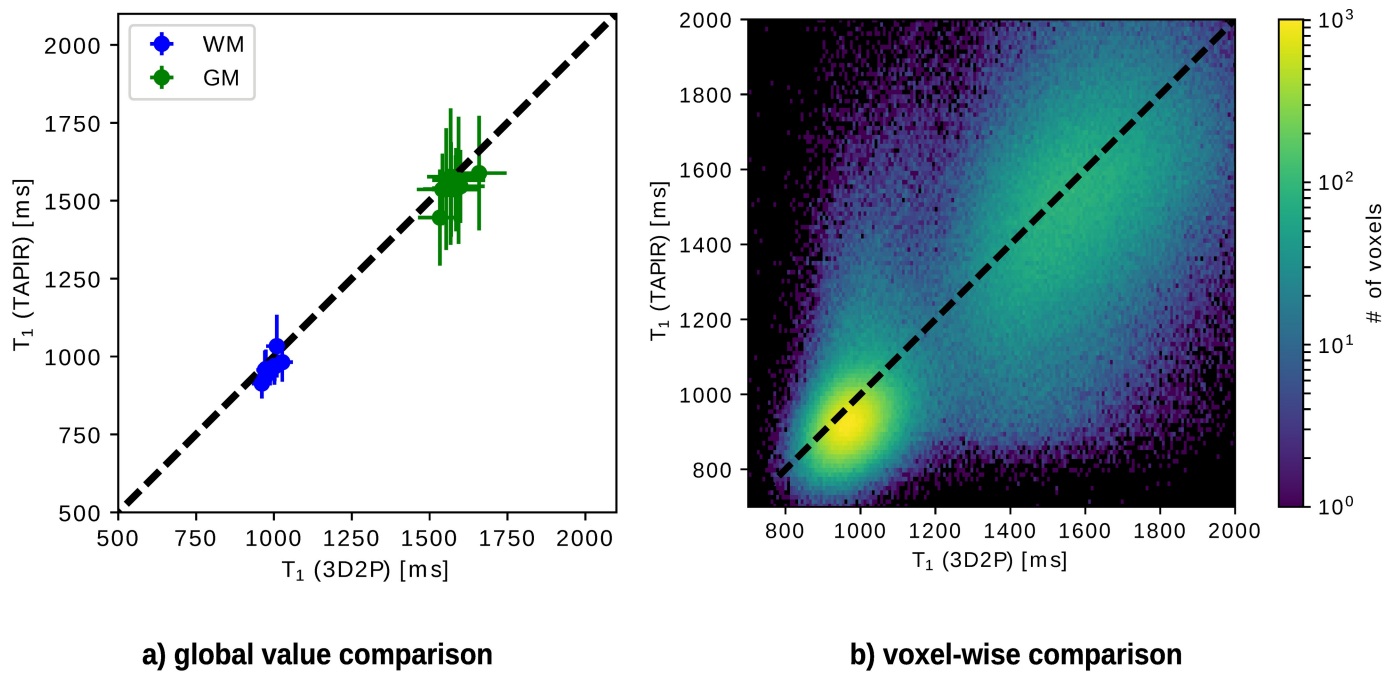**a) global value comparison** **b) voxel-wise comparison**

Fig 7. Analytical comparison of T$_1$ using the 3D2P method and TAPIR as gold standard. a) Shows the global correlation between 3D2P and TAPIR, while b) depicts the corresponding voxel-wise comparison.

https://doi.org/10.1371/journal.pone.0201013.g007

Table 3. Comparison of quantitative T_1 values measured with 3D2P and TAPIR.

tissue type	T_1 (3D2P) [ms]	T_1 (TAPIR) [ms]
WM	988±21	970±35
GM	1580±35	1544±38

simplicity of the method—measurement-wise as well as in post-processing—make it well-suited to be a reference H_2O mapping method.

A recent publication reports that Look-Locker methods systematically underestimate the quantitative T_1 values [32], which we correct for by using an additional inversion efficiency measurement. We note here that TAPIR which is a Look-Locker methods was originally tested against non-selective spectroscopic measurements and was proved to be reliable and accurate. Thus, here we have used TAPIR as the gold standard.

Other quantitative 3D imaging methods report only T_1 and PD (e.g. [15,24,30,33,34]), but quantitative mapping of H_2O is important when it comes to pathology mapping. Although H_2O and T_1 are known to be correlated [35], information about H_2O is unambiguous which is especially important for finding the cause of systematic changes [3]. Additionally, in the 3D2P approach, the transmit field itself is mapped rather than calculated as in other approaches [14,15].

Phantom measurement show that the 3D2P method is suitable for use in mapping all tissue relevant values, demonstrating it as an accurate method for *in vivo* mapping. As the B_1^- correction in SPM is based on brain tissue classification, it does not perform well on phantoms. In actual *in vivo* experiments, the accuracy is expected to be improved. Despite this imperfect correction, results for both, T_1 and H_2O, match reasonably with their corresponding reference values. In particular, the tubes representing living WM and GM show good agreement with the expected values. The T_1 values in GM and especially CSF are overestimated (cf. Fig 2 tubes 7 and 8). The influence of the T_1 bias on H_2O is addressed by error propagation analysis (cf. S3 Text), yielding an error in H_2O of approximately 0.3% in WM, 1.4% in GM and 3.6% in CSF. However, since the M_0 map is normalised to 100% water based on the lateral ventricles, which consist of nearly 100% H_2O, the propagated bias in CSF is theoretical. During the normalisation, the CSF value of the H_2O map is defined to be correct. Nevertheless does the T_1 bias influence WM and GM in that a normalisation factor which is decreased by 3.6% lead to increased H_2O values in tissue.

The reliability of the method was assessed using test-retest measurements. The very small standard deviations of the overall mean values and the corresponding coefficients of variation of each quantitative parameter (cf. S2 Table) demonstrate that the error of the method is well below the population variability in our ten volunteers (cf. Tables 1, 3 and 5). This makes the method suitable for detecting longitudinal changes within single subjects.

The *in vivo* results of the comparison study are in good agreement with established gold standard imaging methods. Small differences in H_2O of GM caused by PVE are observable. Due to the lower resolution of the long TR method, voxels close to CSF show an increased H_2O value, leading to a higher GM mean value. Additionally, T_1 values from TAPIR showed a slightly larger standard deviation than the T_1 values obtained from 3D2P, which is due to the slightly increasing deviation with T_1 value, as reported in [7]. We point out that there is a small but systematic discrepancy between the T_1 values obtained with TAPIR and with the two-point method. An effect which can be expected to influence T_1 quantification very significantly is insufficient spoiling of the transversal magnetisation, as clearly discussed by Preibisch and Deichmann [12]. The signal equation (cf. Eq 1) describes a fully-spoiled GRE sequence and any effects outside this model are not properly taken into account. We have chosen a relatively
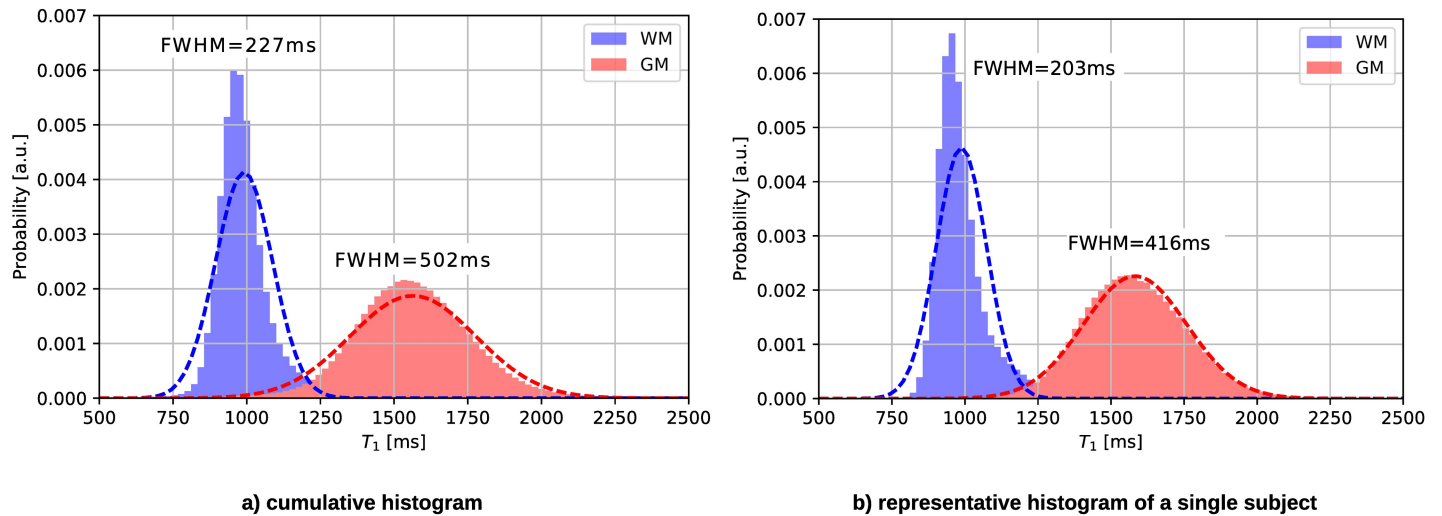
| a) cumulative histogram | b) representative histogram of a single subject |

Fig 8. T_1 histograms of a) all subjects and b) a representative subject measured using the 3D2P method.

https://doi.org/10.1371/journal.pone.0201013.g008

long TR value of 50ms in order to minimise such contributions, but their existence can be expected. Such effects would be more pronounced for longer T_1 values (at similar T_2^*) and for larger flip angles.

Given the fact that the disagreement between the T_1 mapping methods is small, whereas non-optimal spoiling can lead to completely erroneous values[12], we assume that spoiling is close to optimal and could be even further improved by increasing the TR value. Due to measurement time constraints, this is hardly feasible at 3T. At higher fields, higher acceleration factors for parallel imaging can be used and longer TR values employed. However, the relaxation times also change, and a new optimisation would be necessary. Another possible cause for discrepancies are the different optimisations of the methods (see S1 Text and [7]) and different SNR of the data, leading to different systematic deviations from the ground truth values. And yet another possible cause for discrepancies are different, sequence and parameter-specific contributions of magnetisation transfer effects to the observed T_1 values (see e.g. [36,37]). The existence of these effects is well known, but their quantification is challenging. All mentioned

Table 4. Estimated T_1 and corresponding literature values in selected GM regions.

GM region	T1 [ms]	literature values [ms]
temporal lobe	1708±59	1579±86 [27]
frontal lobe	1618±81	1609±86 [24]
		1703±53 [28]
occipital lobe	1650±110	1642±103 [24]
		1820±114 [29]
parietal lobe	1664±80	1690±85 [24]
caudate (head)	1535±64	1584±92 [24]
		1483±42 [30]
putamen	1448±71	1483±78 [24]
		1337±42 [30]
		1362±75 [12]
thalamus	1475±71	1549±108 [24]
		1216±40 [26]

https://doi.org/10.1371/journal.pone.0201013.t004
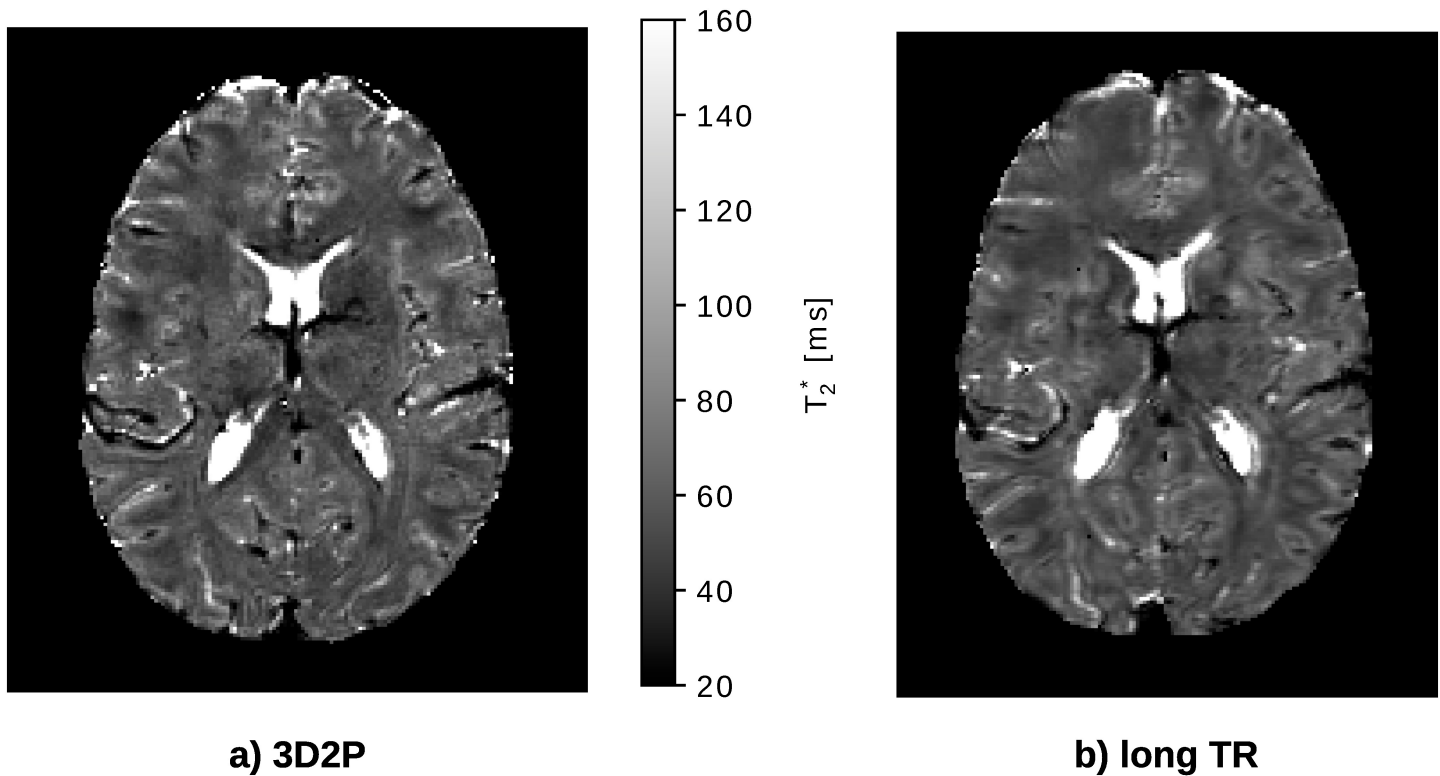
a) 3D2P   **b) long TR**

Fig 9. *In vivo* comparison of the quantitative T2* maps using the 3D2P and long TR method. The dotted line represents the Gaussian fit to the histograms.

effects can also contribute to the accuracy of water content values. We have investigated the question of whether the noticed T_1 discrepancies, whatever their source, can account for the discrepancies in the measured water content.

We point out that both signals (7 and 40˚) are needed for the derivation of T_1, whereas water content values are determined, in our processing chain, only from the lower flip-angle signal. We therefore assume that the gold standard methods for H_2O and T_1, which are fully independent from each other, deliver accurate results, and that the small deviation in T_1 values could be due to the insufficiently accurate description of the signal with large flip angle (40˚).

A detailed ROI analysis yields excellent agreement with literature values for both, T_1 and H_2O. Especially for H_2O and T_1, the cumulative histogram shows clearly distinguishable peaks. The comparisons between the cumulative and single subject histograms show only a minor increase in full width half maximum of the distributions. This reflects the small range of physiological variation of the mean T_1 values in our collective of ten male volunteers with narrowly defined age. As shown by the test-retest comparison, the reliability of the method is higher than this physiological variability and adequate to investigate variation of the mean T_1 values with e.g. age or pathological change.

In general, it is difficult to find a gold standard method for T_2^* mapping. It can be expected, however, that a 3D method with a small voxel size yields the best possible results as de-phasing effects are minimised and more anatomical details can be imaged (cf. Fig 9). The long TR method yields generally higher SNR in the T_2^* maps due to the use of the full magnetisation (TR = 10s, α = 90˚) and a higher number of echoes (32 echoes). As the maximum echo time is generally higher using the long TR reference method, the accuracy of the fit for regions with comparably long T_2^*, i.e. CSF in particular, is improved. Differences in the T_2^* values are

a) global value comparison   **b) voxel-wise comparison**
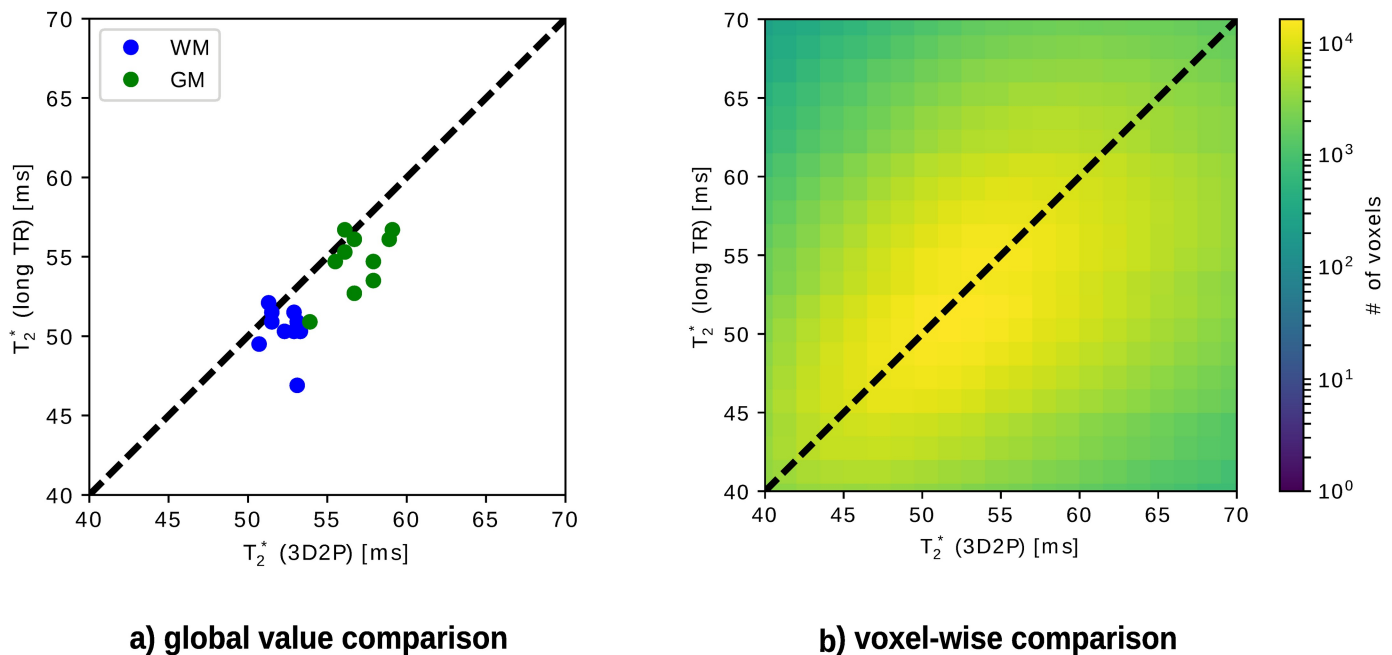
Fig 10. Analytical comparison of T2* using the 3D2P method and long TR as the gold standard. a) shows the global correlation between 3D2P and long TR, while b) depicts the corresponding voxel-wise comparison.

expected not only due to the different voxel size but also due to different effects of the B_0 field inhomogeneities on signal evolution with echo time in 3D and 2D imaging. The signal decay in voxels with long T_2 (and thus T_2^*) are better characterised using a long echo train, which is better possible with a long TR [38]. The TR value chosen for the 3D mapping method was a compromise between allowed length of the echo train and measurement time constraints. For regular WM/GM T_2^* values, sampling of the signal decay covers the first T_2^* interval. For CSF, however, a much longer sampling time would be required, which is very difficult in a 3D method. The fit quality is therefore reduced for voxels with long T_2^*. The difference in the mean values for bulk WM and GM obtained with the two methods is probably mainly due to the difference in voxel size. The 2D long TR method has a voxel size of 2.25 (1×1.5×1.5 vs 1×1×1) times larger than the 1mm^3 of the 3D acquisition, and increased dephasing within the voxel is expected to lead to a decrease in T_2^*.

For a fair comparison, however, the same number of echoes, echo spacing and BW should be used in the 2D and 3D acquisitions. This was not the case here, since the parameters of the two methods were optimised separately mainly based on considerations regarding H_2O accuracy and reliability. The bandwidth used in the 3D method (BW = 650Hz/px) was chosen empirically as a compromise of an increase in SNR due to a higher number of echoes and a decrease due to the dependency of SNR on the square root of BW.

Multi-parametric MR imaging shows its power, not only in oncology [39], but also at refining our current understanding of the structural organisation of the human brain [40].

Table 5. Comparison of quantitative T2* values measured with 3D2P and long TR.

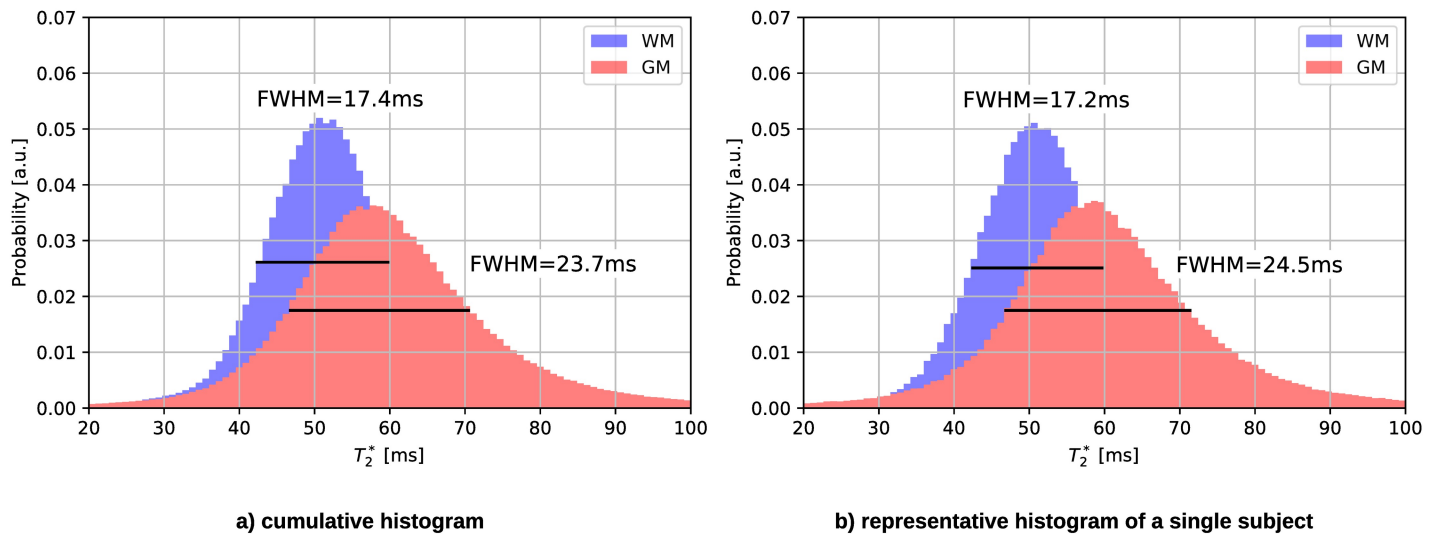| tissue type	T2* (3D2P) [ms]	T2* (long TR) [ms]
WM	52±1	50±1
GM	57±2	55±2

Fig 11. T_2^* histograms of a) all subjects and b) a representative subject measured using the 3D2P method. The dotted line represents the Gaussian fit to the histograms.

Quantitative multi-parametric MRI can be reasonably expected to bring this analytical power to a new level. The 3D2P method provides accurate information on some of the most fundamental MR parameters (magnetisation density of water, T_1 and T_2^*). A strong correlation between water content and the longitudinal relaxation time T_1 in brain tissue exists, as reported nearly two decades ago [35]. It has been used in a number of studies to infer water content in brain tissue from measured T_1 values and recently exploited to correct proton density maps for receiver inhomogeneity effects and convert them to water content (e.g. [9,41]).

To conclude, using a 3D2P method with the parameter set presented, it was possible to present a robust imaging method that allows high-resolution, isotropic and quantitative imaging of the human brain. Even though numerous quantitative imaging methods have already been presented (e.g.[1,2,8,9,13,14,25,26,28,29,33,34,31,42]), this 3D approach is advantageous due to higher SNR at high resolution, whole brain coverage, high reliability, as demonstrated by the test-retest measurements and good accuracy, as can be inferred from the *in vivo* comparison to gold standard methods as well as phantom validation. Critical elements to achieving its quantitative power are improved B_1^+ correction due to measurements using AFI, a long TR value, matching tissue T_2^* and reducing contributions from unspoiled magnetisation, as well as the use of a large number of echoes, both for T_2^* and T_1 mapping. An even longer TR would further improve the characterisation of the CSF signal, and the quantitative power of the method, however, at the expense of measurement time. This might become feasible at higher fields where higher acceleration factors for parallel imaging can be employed. It is arguable that the total acquisition time of approx. 22 minutes is too long for clinical applications. However, when changing the resolution of the chosen gold standard methods to approximately match the one of 3D2P, the gold standards' acquisition times increase to approximately the same order of magnitude. We report here results obtained with an isotropic 1mm resolution that is well suited for anatomical characterisation. The measurement time with a 3D method is easily adapted to measurement time requirements by slightly modifying the resolution. Given that we use a phase as well as a slice encoding direction, small modifications to the resolution in each of these directions can significantly reduce the measurement time.

During post-processing of the 3D2P results the following assumptions are made: The meGRE signal equation, which implies perfect spoiling, is correct and both meGREs are modulated by the same T_1. Magnetisation transfer effects due to direct saturation are neglected. In future work, it remains to be investigated whether this assumptions have a significant impact on the estimated quantities. By using two meGRE with magnitude and phase data, susceptibility and conductivity mapping becomes possible. Additionally, the method can easily be extended by measuring magnetic transfer ratio, which is a challenging task in 2D imaging. Future work might also include measurements at high fields, suppressing physiological motion and extracting a macromolecular content map. Moreover, the correlation between all quantitative parameters can be investigated in more detail.

Supporting information

S1 Text. Parameter optimisation. Description of the Monte Carlo simulations.
(DOCX)

S2 Text. Test-retest measurements. Description of the test-retest measurements.
(DOCX)

S3 Text. Error propagation analysis. Derivation of the error propagation of T_1.
(DOCX)

S1 Fig. Parameter optimisation for the 3D2P method when TR1 = TR2 = 50ms and SNR = 20. Dependence on α_1 and α_2 of: a) ΔH_2O, b) std dev H_2O, c) ΔT_1, d) std dev T_1. Only the combinations of parameters are shown for which a-d remain below 10%.
(TIF)

S2 Fig. Test-retest measurements of the presented 3D2P method, yielding global mean values of a) H_2O, b) T_1 and c) T_2^* at each time point. Global mean values of WM and GM were calculated individually, using the tissue probability maps provided in SPM with a threshold of 99%. Thus, the shown error bars indicate the corresponding standard deviation over all voxels included in the probability masks for each given time point.
(TIF)

S1 Table. Results of the test-retest measurements, yielding global mean values for all quantitative parameters at each time point (TP). Global mean values of WM and GM were calculated individually, using the tissue probability maps provided in SPM with a threshold of 99%. Thus, the listed errors indicate the corresponding standard deviation over all voxels included in the probability masks for each given time point.
(DOCX)

S2 Table. Overall mean and standard deviation (std dev) of all ten time points of the test-retest measurements. The intra-subject coefficient of variation (CV) is given as fraction of the standard deviation over the overall mean (CV in percentage).
(DOCX)

Acknowledgments

Author Contributions

Conceptualization: N. Jon Shah, Ana-Maria Oros-Peusquens.

Formal analysis: Melissa Schall, Markus Zimmermann, Yun Gu.

Funding acquisition: N. Jon Shah.

Investigation: Melissa Schall, Elene Iordanishvili, Ana-Maria Oros-Peusquens.

Methodology: Ana-Maria Oros-Peusquens.

Project administration: N. Jon Shah, Ana-Maria Oros-Peusquens.

Resources: N. Jon Shah.

Software: Melissa Schall, Markus Zimmermann.

Supervision: N. Jon Shah, Ana-Maria Oros-Peusquens.

Validation: Melissa Schall, Elene Iordanishvili, Ana-Maria Oros-Peusquens.

Visualization: Melissa Schall.

Writing – original draft: Melissa Schall, Markus Zimmermann.

Writing – review & editing: Melissa Schall, Markus Zimmermann, Elene Iordanishvili, Yun Gu, N. Jon Shah, Ana-Maria Oros-Peusquens.

References

1. Badve C, Yu A, Dastmalchian S, Rogers M, Ma D, Jiang Y, et al. MR fingerprinting of adult brain tumors: Initial experience. Am J Neuroradiol. 2017; 38(3):492–9. https://doi.org/10.3174/ajnr.A5035 PMID: 28034994

2. Oros-Peusquens AM, Keil F, Langen KJ, Herzog H, Stoffels G, Weiss C, et al. Fast and accurate water content and T2* mapping in brain tumours localised with FET-PET. Nucl Instruments Methods Phys Res Sect A Accel Spectrometers, Detect Assoc Equip. Elsevier; 2014; 734(PART B):185–90.

3. Tofts P. Quantitative MRI of the Brain. John Wiley & Sons Inc; 2003.

4. Shah NJ, Neeb H, Zaitsev M, Steinhoff S, Kircheis G, Amunts K, et al. Quantitative T1 Mapping of Hepatic Encephalopathy Using Magnetic Resonance Imaging. Hepatology. 2003; 38(5):1219–26. https://doi.org/10.1053/jhep.2003.50477 PMID: 14578860

5. Reetz K, Abbas Z, Costa AS, Gras V, Tiffin-Richards F, Mirzazade S, et al. Increased Cerebral Water Content in Hemodialysis Patients. PLoS One. 2015; 10(3).

6. Shah NJ, Neeb H, Kircheis G, Engels P, Häussinger D, Zilles K. Quantitative cerebral water content mapping in hepatic encephalopathy. Neuroimage. 2008; 41(3):706–17. https://doi.org/10.1016/j.neuroimage.2008.02.057 PMID: 18456518

7. Shah NJ, Zaitsev M, Steinhoff S, Zilles K. A new method for fast multislice T(1) mapping. Neuroimage. 2001; 14(5):1175–85. https://doi.org/10.1006/nimg.2001.0886 PMID: 11697949

8. Steinhoff S, Zaitsev M, Zilles K, Shah NJ. Fast T 1 Mapping With Volume Coverage. Magn Reson Med. 2001; C:131–40.

9. Abbas Z, Gras V, Möllenhoff K, Oros-Peusquens A-M, Shah NJ. Quantitative water content mapping at clinically relevant field strengths: A comparative study at 1.5T and 3T. Neuroimage. 2015; 106:404–13. https://doi.org/10.1016/j.neuroimage.2014.11.017 PMID: 25463455

10. Helms G, Dathe H, Weiskopf N, Dechent P. Identification of signal bias in the variable flip angle method by linear display of the algebraic ernst equation. Magn Reson Med. 2011; 66(3):669–77. https://doi.org/10.1002/mrm.22849 PMID: 21432900

11. Gras V, Abbas Z, Shah J. Spoiled FLASH MRI with Slice Selective Excitation: Signal Equation with a Correction Term. Concepts Magn Reson Part A. 2013; 42A(April):89–100.

12. Preibisch C, Deichmann R. Influence of RF spoiling on the stability and accuracy of T1 mapping based on spoiled FLASH with varying flip angles. Magn Reson Med. 2009; 61(1):125–35. https://doi.org/10.1002/mrm.21776 PMID: 19097220

13. Deoni SCL, Peters TM, Rutt BK. High-resolution T1 and T2 mapping of the brain in a clinically accept-able time with DESPOT1 and DESPOT2. Magn Reson Med. 2005; 53(1):237–41. https://doi.org/10.1002/mrm.20314 PMID: 15690526

14. Volz S, Nöth U, Jurcoane A, Ziemann U, Hattingen E, Deichmann R. Quantitative proton density map-ping: Correcting the receiver sensitivity bias via pseudo proton densities. Neuroimage. 2012; 63 (1):540–52. https://doi.org/10.1016/j.neuroimage.2012.06.076 PMID: 22796988

15. Palma G, Tedeschi E, Borrelli P, Cocozza S, Russo C, Liu S, et al. A novel multiparametric approach to 3D quantitative MRI of the brain. PLoS One. 2015; 10(8):1–20.

16. Yarnykh VL. Actual flip-angle imaging in the pulsed steady state: A method for rapid three-dimensional mapping of the transmitted radiofrequency field. Magn Reson Med. 2007; 57(1):192–200. https://doi.org/10.1002/mrm.21120 PMID: 17191242

17. Friston KJ, Ashburner JT, Kiebel SJ, Nichols TE, Penny WD. Statistical parametric mapping—the anal-ysis of functional brain images. 1st ed. EBook WPKFJASKTN, editor. Elsevier Ltd.; 2006.

18. Oros-Peusquens a. M, Laurila M, Shah NJ. Magnetic field dependence of the distribution of NMR relax-ation times in the living human brain. Magn Reson Mater Physics, Biol Med. 2008; 21(1–2):131–47. https://doi.org/10.1007/s10334-008-0107-5 PMID: 18338191

19. Rooney WD, Johnson G, Li X, Cohen ER, Kim SG, Ugurbil K, et al. Magnetic field and tissue dependen-cies of human brain longitudinal 1H2O relaxation in vivo. Magn Reson Med. 2007; 57(2):308–18. https://doi.org/10.1002/mrm.21122 PMID: 17260370

20. Dmitry A, Yablonski E, Haacke EM. NMR Signal Behavior in Magnetic ally Inhomogeneous Tissues: The Static Dephasing Regime. Magn Reson Med. 1994;(32):749–63. PMID: 7869897

21. Yablonskiy DA, Sukstanskii AL, Luo J, Wang X. Voxel spread function method for correction of mag-netic field inhomogeneity effects in quantitative gradient-echo-based MRI. Magn Reson Med. 2013; 70 (5):1283–92. https://doi.org/10.1002/mrm.24585 PMID: 23233445

22. Ashburner J, Friston KJ. Unified segmentation. Neuroimage. 2005; 26(3):839–51. https://doi.org/10.1016/j.neuroimage.2005.02.018 PMID: 15955494

23. Millman KJ, Aivazis M. Python for scientists and engineers. Comput Sci Eng. 2011; 13(2):9–12.

24. Abbas Z, Gras V, Möllenhoff K, Keil F, Oros-Peusquens AM, Shah NJ. Analysis of proton-density bias corrections based on T1 measurement for robust quantification of water content in the brain at 3 Tesla. Magn Reson Med. 2014; 1745:1735–45.

25. Warntjes JBM, Dahlqvist O, Lundberg P. Novel method for rapid, simultaneous T1, T2*, and proton density quantification. Magn Reson Med. 2007; 57(3):528–37. https://doi.org/10.1002/mrm.21165 PMID: 17326183

26. Whittall KP, Mackay AL, Graeb DA, Nugent RA, Li DKB, Paty DW. In vivo measurement ofT2 distribu-tions and water contents in normal human brain. Magn Reson Med. 1997; 37(1):34–43. PMID: 8978630

27. Abbas Z, Ridder D, Dzieciol K, Shah NJ. Validation of CSF based calibration for accurate and robust quantification of water content [abstract]. ISMRM Honolulu. 2017;vol 25:abstract nr 1454.

28. Cheng K, Koeck PJB, Elmlund H, Idakieva K, Parvanova K, Schwarz H, et al. Rapid High-Resolution T1 Mapping by Variable Flip Angles: Accurate and Precise Measurements in the Presence of Radiofre-quency Field Inhomogeneity. Magn Reson Med. 2006; 37(55):566–76.

29. Stanisz GJ, Odrobina EE, Pun J, Escaravage M, Graham SJ, Bronskill MJ, et al. T1, T2 relaxation and magnetization transfer in tissue at 3T. Magn Reson Med. 2005; 54(3):507–12. https://doi.org/10.1002/mrm.20605 PMID: 16086319

30. Gelman Neil, 1 Ewing James R., 1 Gorell Jay M., 1* Spickler Eric M. 2, Solomon1 and EG, Kiviniemi V, Jauhiainen J, Tervonen O, Pääkkö E, et al. Interregional Variation of Longitudinal Relaxation Rates in Human Brain at 3.0 T: Relation to Estimated Iron and Water Contents. Neuroimage. 2013; 44(1):137–41.

31. Ma D, Gulani V, Seiberlich N, Liu K, Sunshine JL, Duerk JL, et al. Magnetic resonance fingerprinting. Nature. 2013; 495(7440):187–92. https://doi.org/10.1038/nature11971 PMID: 23486058

32. Stikov N, Boudreau M, Levesque IR, Tardif CL, Barral JK, Pike GB. On the accuracy of T1 mapping: Searching for common ground. Magn Reson Med. 2015; 73(2):514–22. https://doi.org/10.1002/mrm.25135 PMID: 24578189

33. Deichmann R. Fast high-resolution T1 mapping of the human brain. Magn Reson Med. 2005; 54(1):20–7. https://doi.org/10.1002/mrm.20552 PMID: 15968665

34. Sabati M, Maudsley AA. Fast and high-resolution quantitative mapping of tissue water content with full brain coverage for clinically-driven studies. Magn Reson Imaging. 2013; 31(10):1752–9. https://doi.org/10.1016/j.mri.2013.08.001 PMID: 24050900

35. Fatouros PP, Marmarou A. Use of magnetic resonance imaging for in vivo measurements of water content in human brain: method and normal values. J Neurosurg. 1999; 90(1):109–15. https://doi.org/10.3171/jns.1999.90.1.0109 PMID: 10413163

36. Wolff SD, Balaban RS. Magnetization transfer contrast (MTC) and tissue water proton relaxation in vivo. Magn Reson Med [Internet]. 1989; 10(1):135–44. Available from: http://doi.wiley.com/10.1002/mrm.1910100113 PMID: 2547135

37. Turner R, Oros-Peusquens AM, Romanzetti S, Zilles K, Shah NJ. Optimised in vivo visualisation of cortical structures in the human brain at 3 T using IR-TSE. Magn Reson Imaging. 2008; 26(7):935–42. https://doi.org/10.1016/j.mri.2008.01.043 PMID: 18524522

38. Preibisch C, Volz S, Anti S, Deichmann R. Exponential excitation pulses for improved water content mapping in the presence of background gradients. Magn Reson Med. 2008; 60(4):908–16. https://doi.org/10.1002/mrm.21730 PMID: 18816811

39. Hoeks CCM a, Barentsz JO, Hambrock T, Yakar D, Somford DM, Heijmink SWTPJ, et al. Prostate cancer: multiparametric MR imaging for detection, localization, and staging. Radiology. 2011; 261(1):46–66. https://doi.org/10.1148/radiol.11091822 PMID: 21931141

40. Glasser MF, Coalson TS, Robinson EC, Hacker CD, Yacoub E, Ugurbil K, et al. A Multi-Modal Oarcellation of Human Cerebral Cortex. Nature. 2017; 536(7615):171–8.

41. Baudrexel S, Reitz SC, Hof S, Gracien RM, Fleischer V, Zimmermann H, et al. Quantitative T1and proton density mapping with direct calculation of radiofrequency coil transmit and receive profiles from two-point variable flip angle data. NMR Biomed. 2016; 29(3):349–60. https://doi.org/10.1002/nbm.3460 PMID: 26756673

42. Weiskopf N, Suckling J, Williams G, Correia M. MM, Inkster B, Tait R, et al. Quantitative multi-parameter mapping of R1, PD*, MT, and R2* at 3T: A multi-center validation. Front Neurosci. 2013; 7(7 JUN):1–11.